Available online at www.sciencedirect.com
ScienceDirect
Trans. Nonferrous Met. Soc. China 35(2025) 2711−2725
Transactions of Nonferrous Metals Society of China
www.tnmsc.cn

# Effect of B-site Mo doping on electrochemical properties of $La_{0.6}Sr_{0.4}Fe_{0.9}Ni_{0.1}O_{3-\delta}$ cathode materials for proton-conducting solid oxide fuel cells

Ting TING, Di XIE, Li CHEN, Li-jun WANG

Collaborative Innovation Center of Steel Technology, University of Science and Technology Beijing, Beijing 100083, China

Received 14 December 2023; accepted 18 September 2024

**Abstract:** To address the challenge of insufficient oxygen vacancies in proton-conducting solid oxide fuel cells (H-SOFC), transition metal elements were doped into the B site of lanthanum ferrite perovskite ($ABO_3$) to enhance its catalytic activity further. The Mo-doped $La_{0.6}Sr_{0.4}Fe_{0.9-x}Ni_{0.1}Mo_xO_{3-\delta}$ ($LSFNM_x$, $x$=0.05, 0.1) powder was synthesized via the sol−gel method, and its crystal structure, conductivity, defect chemistry, and electrochemical performance as an H-SOFC cathode were investigated. The prepared material exhibited a hexagonal structure with the $R$-3$c$ space group and demonstrates good chemical stability under simulated working conditions. Mo doping increased the surface concentration of oxygen vacancies, leading to the accelerated oxygen transportation. Consequently, the polarization resistance ($R_{pol}$) and activation energy ($E_a$) are reduced. Specifically, $LSFNM_{0.05}$ showed the lowest polarization resistance (approximately 0.26 $\Omega\cdot cm^2$) at 700 °C. $LSFNM_{0.05}$ achieved a maximum power density of 484 $mW/cm^2$ at this temperature, outperforming those of LSFN (353 $mW/cm^2$) and $LSFNM_{0.1}$ (365 $mW/cm^2$).

**Key words:** proton-conducting solid oxide fuel cells; proton transmission; air electrode; doping engineering; electrochemical properties; oxygen vacancy

## 1 Introduction

The global consumption of fossil fuels has increased concerns about energy depletion and ecological environmental issues [1,2]. Hydrogen energy, as a renewable energy source, offers advantages such as high efficiency, cleanliness, safety, and environmental friendliness, making it widely adopted in the new energy industry [3]. It represents a strategic direction in human energy development. Solid oxide fuel cells (SOFCs) stand out among fuel cell technologies as zero-carbon emission, clean, and efficient energy conversion devices [4,5]. They boast significant advantages, including high power density, compatibility with a wide range of fuel gases ($H_2$, $CH_4$, $NH_3$, etc.), and low cost [6−9]. However, traditional SOFCs face challenges of low efficiency and high costs when operating at high temperatures. Consequently, SOFC research is shifting towards low-temperature operating conditions. Proton-conducting solid oxide fuel cells (H-SOFCs) exhibit excellent conductivity at lower temperatures due to the smaller radius of $H^+$ (0.25 Å) compared to that of $O^{2-}$ (0.74 Å) and lower activation energy [10,11]. Proton ceramic fuel cells (PCFCs), a type of H-SOFC, demonstrate efficient operation at relatively low temperatures (400−700 °C) [12], outperforming traditional SOFC analogues. This characteristic enhances the stability of battery components when using composite oxygen electrodes and indicates promising prospects for

**Corresponding author:** Li-jun WANG, Tel: +86-10-62333622, E-mail: lijunwang@ustb.edu.cn
https://doi.org/10.1016/S1003-6326(25)66842-7

PCFC applications [13,14].

Current research primarily focuses on developing high-efficiency, low-cost, and stable cathode materials [15]. Recent literature [16−19] has reported significant advancements in this area. For instance, $La_{0.5}Sr_{0.5}Co_{0.95}Nb_{0.05}O_{3-\delta}$, a solid oxide symmetric electrode material with a thin-film perovskite structure, has been successfully synthesized through sputtering. With a thickness of approximately 200 nm, this symmetric electrode achieved a maximum power density of 390 mW/cm$^2$ at 700 °C [16]. While cobalt-based perovskite oxides have been widely used as PCFC cathodes, they often suffer from poor thermo-mechanical compatibility with electrolytes and limited structural stability. In contrast, triple conductive perovskite-based nanocomposites have shown promise as PCFC cathodes, exhibiting high catalytic activity and stability. These materials have demonstrated an impressive power density of 829 mW/cm$^2$ at 650 °C [17]. An IT-SOFC utilizing an LSFN cathode, $BaZr_{0.1}Ce_{0.7}Y_{0.2}O_{3-\delta}$ electrolyte, and Ni-$BaZr_{0.1}Ce_{0.7}Y_{0.2}O_{3-\delta}$ anode substrate, prepared via a simple spin coating process, achieved the maximum power densities of 405, 238, and 140 mW/cm$^2$ at 700, 650, and 600 °C, respectively [18]. However, the power density of the battery at low temperatures is still relatively low. Therefore, it is necessary to find new transition metal elements for doping. LU et al [19] developed a Mo-doped cathode material, $Pr_{0.6}Sr_{0.4}Fe_{0.7}Ni_{0.2}Mo_{0.1}O_{3-\delta}$, using an improved synthesis method. Their experimental results revealed that the introduction of Mo significantly enhanced the oxygen reduction reaction (ORR) activity of the cathode. At 800 °C, $Pr_{0.6}Sr_{0.4}Fe_{0.7}Ni_{0.2}Mo_{0.1}O_{3-\delta}$ had a maximum power density of 500 mW/cm$^2$, outperforming that of PSFN (400 mW/cm$^2$). Moreover, the Mo-doped material exhibited a reduced coefficient of thermal expansion, improving its compatibility with the electrolyte.

Although LSF-based perovskite material has high electrical conductivity and electrochemical activity, it lacks certain ORR activity when used as a fuel cell cathode. Meanwhile, the adsorption and dissociation of oxygen cannot meet the high requirements. Therefore, to improve their stability of the structure and the catalytic activity, $La_{0.6}Sr_{0.4}Fe_{0.9}Ni_{0.1}O_{3-\delta}$ (LSFN), $La_{0.6}Sr_{0.4}Fe_{0.85}Ni_{0.1}Mo_{0.05}O_{3-\delta}$ ($LSFNM_{0.05}$), and $La_{0.6}Sr_{0.4}Fe_{0.8}Ni_{0.1}Mo_{0.1}O_{3-\delta}$ ($LSFNM_{0.1}$) powders were prepared using the sol−gel method in this work. Subsequently, the impact of Mo doping on cathode materials' structure, conductivity, distribution of relaxation time (DRT), and electrochemical properties was studied.

## 2 Experimental

### 2.1 Material synthesis

$La_{0.6}Sr_{0.4}Fe_{0.9-x}Ni_{0.1}Mo_xO_{3-\delta}$ ($LSFNM_x$) cathode material was synthesized by the sol−gel method. Stoichiometric $La(NO_3)_3·6H_2O$, $Sr(NO_3)_2$, $Fe(NO_3)_3·9H_2O$, $Ni(NO_3)_2·6H_2O$ and $(NH_4)_6Mo_7O_{24}·9H_2O$ were dissolved into DI water containing an amount of citric acid (CA) and ethylenediaminetetraacetic acid (EDTA). The solution was heated at 80 °C under stirring until the colloidal solution was obtained. The precursor was dried at 200 °C for 12 h and then pretreated in air at 600 °C for 2 h. Finally, the obtained powder was calcined in air at 1100 °C for 5 h to get pure perovskite oxides. $BaZr_{0.1}Ce_{0.7}Y_{0.1}Yb_{0.1}O_{3-\delta}$ (BZCYYb) electrolyte powder was prepared by the traditional solid-state reaction method, which can be found in our previous work [20].

### 2.2 Cell fabrication

2.2.1 Single cell

Single cells with NiO−BZCYYb|BZCYYb (1% NiO)|$LSFNM_x$ ($x$=0, 0.05, 0.1) for electrochemical performance research were fabricated by spraying method. After grinding 13 g of BZCYYb, 7 g of NiO, and 20 g of cornstarch for 5 h, the mixture was dried at 80 °C to obtain the anode powder. 0.4−0.5 g of the anode dry powder was pressed into 15 mm diameter slices under 8 MPa and then sintered in a muffle furnace at 1000 °C for 2 h to obtain the required anode disks. 0.99 g of pure phase BZCYYb powder, 0.01 g of NiO, and 20 mL of ethylene glycol were mixed, and then ball-milled for 5 h. The obtained slurry was sprayed onto the anode disks and calcined at 1450 °C for 5 h. A half cell with the structure of NiO−BZCYYb|BZCYYb was obtained. The cathode powders were ball-milled with the mixture of isopropanol, ethylene glycol, and glycerin (volume ratio of 1:10:2:1) for 1 h. Then, the cathode slurry was sprayed on the obtained half-cell with an effective area of 0.26 cm$^2$ and sintered for 2 h at 1000 °C. Finally, Ag paste was coated on both sides of the cell as collectors.

2.2.2 Symmetric cell

Dense BZCYYb electrolyte disks were prepared by pressing BZCYYb powder into slices with a diameter of 15 mm and sintered at 1450 °C for 5 h. The BZCYYb disks were polished to a thickness of 300 μm using SiC sandpaper before cell preparation. The cathode slurry was symmetrically sprayed on both sides of the BZCYYb disk with an active area of 0.26 $cm^2$. The symmetric cell was fired at 1050 °C for 2 h in air to obtain a porous electrode.

### 2.3 Characterization

The phase structure of synthetic materials was studied by X-ray diffraction (XRD). The sample was treated in a wet Ar−21%$O_2$ atmosphere at 800 °C for 20 h to investigate the chemical stability in the working atmosphere. The collected data were subjected to Rietveld refinement using GSAS software to determine the lattice parameters precisely. The micromorphologies of powders and cells were studied using a field-emission SEM (FESEM). The valence states of elements on the particle surface of $LSFNM_x$ and LSFN were tested by X-ray photoelectron spectroscopy (XPS). At 284.8 eV, all peak positions were corrected by C 1s peak. When the thermogravimetric test was carried out, the sample with a mass of about 50 mg was placed in the $Al_2O_3$ crucible in an argon atmosphere. To test the conductivity, the electrode powder was ground with a certain amount of polyvinyl alcohol solution, uniaxial dry pressed into a rectangular bar with a size of 2 mm × 5 mm × 20 mm, and then annealed in air for 5 h at 1400 °C. The conductivities of electrode rods in wet and dry air were measured at 300−800 °C with an interval of 50 °C using a DC four-probe method on the Keithley 2460 equipment.

### 2.4 Electrochemical test

The current density−voltage ($J$−$V$) relationship and EIS impedance spectrum of the battery at 550−700 °C were recorded by a PARSTAT 2273 precision electrochemical workstation. The DRT analysis was performed on the initial impedance spectra data. For the DRT calculation, the DRT code was available from a free MATLAB GUI (DRT tools), and the basis Gaussian function was used. The cathode was exposed to air, and the anode was supplied with $H_2$ (3% $H_2O$; $H_2$ flow rate: 30 mL/min) as the fuel during the stability test of the single cells.

## 3 Results and discussion

### 3.1 Phase constitution of materials

Figure 1(a) shows the XRD results of the three materials synthesized via the sol−gel method. The $LSFNM_x$ ($x$=0, 0.05, 0.1) exhibits a hexagonal perovskite structure, which remains unaltered upon Mo introduction. Rietveld refinement analysis of $LSFNM_{0.05}$ (Fig. 1(b), $R_p$=2.61%, $R_{wp}$=3.43%, $\chi^2$=6.889) confirms a highly symmetrical $R$-3$c$ space group with lattice parameters $a$=$b$=5.5341 Å and $c$=13.4697 Å. The inset of Fig. 1(a) reveals a shift of the main diffraction peak towards lower angles. This shift, interpreted through Bragg's law ($n\lambda=2d\cdot\sin\theta$) [21], indicates lattice expansion resulting from the partial substitution of $Fe^{4+}$ ions (0.585 Å) with the larger $Mo^{6+}$ ions (0.59 Å). For H-SOFC, the generated protons are transported through the electrolyte to the cathode, where they combine with electrons and $O_2$ molecules to form $H_2O$. Given this mechanism, we evaluated the chemical compatibility between the electrode materials and the electrolyte, as well as the phase stability in humid air. To assess chemical compatibility, electrode and electrolyte powders (1:1 in mass ratio) were sintered in Ar−21%$O_2$ (3% $H_2O$) at 800 °C for 20 h. As shown in Fig. 1(c), the absence of impurity phases demonstrates excellent chemical compatibility between $LSFNM_x$ ($x$=0, 0.05, 0.1) cathodes and BZCYYb electrolyte. Furthermore, Fig. 1(d) illustrates that the electrode materials maintain a stable perovskite structure in humid environments, a crucial attribute for their application in H-SOFC.

The surface morphologies of the as-prepared $LSFNM_{0.05}$ were investigated by SEM. The as-prepared $LSFNM_{0.05}$ showed a relatively smooth surface (Fig. 2(a)). The EDS elemental mapping results in Fig. 2(b) confirmed the homogeneous distribution of La, Sr, Fe, Ni, and Mo components in $LSFNM_{0.05}$, suggesting the successful synthesis of $LSFNM_{0.05}$.

### 3.2 Elemental valence states of materials

The X-ray photoelectron spectroscopy (XPS) experiments were conducted to investigate the composition and chemical valence states of LSFN and Mo-doped samples. Figure 3(a) presents the comparative analysis of the Fe $2p_{3/2}$ spectra for

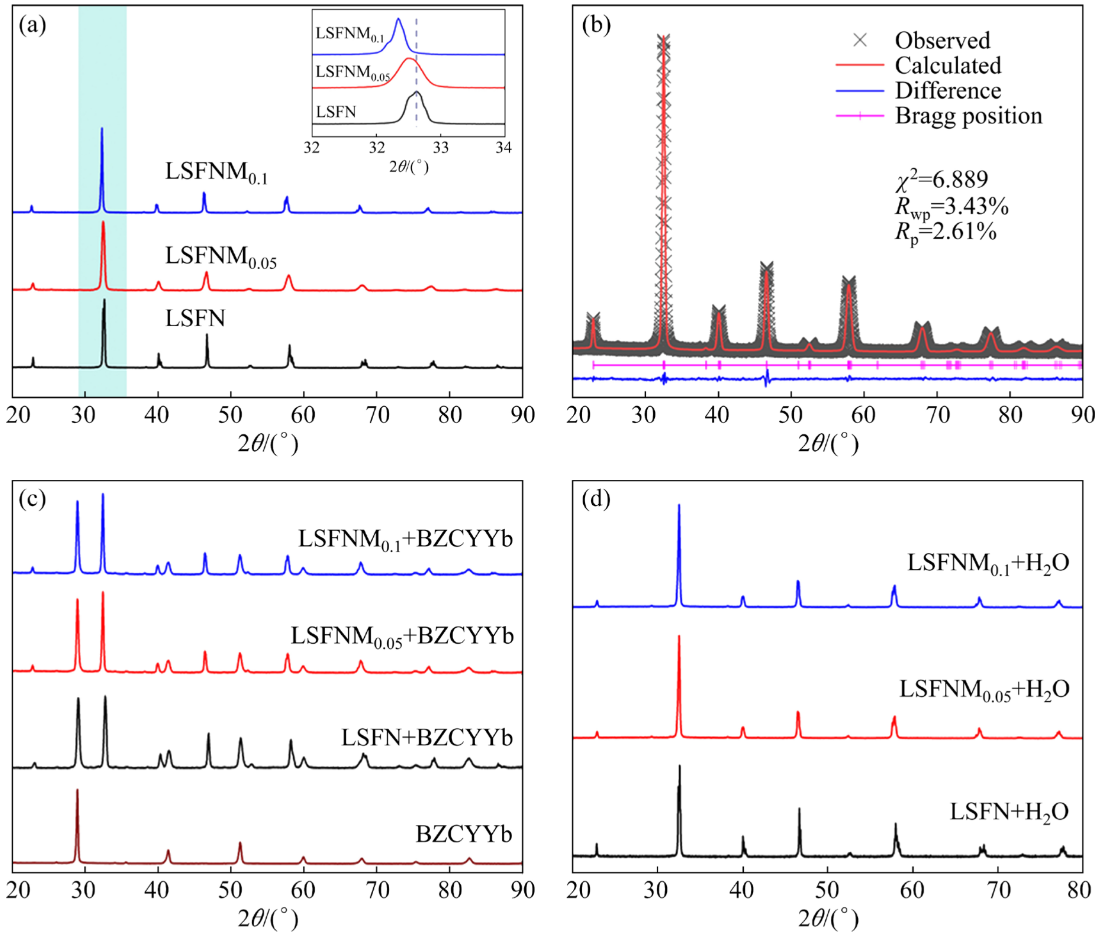


**Fig. 1** (a) XRD patterns of $LSFNM_x$ ($x$=0, 0.05, 0.1); (b) Refined XRD profile of $LSFNM_{0.05}$ powder; (c) Chemical compatibility of $LSFNM_x$ ($x$=0, 0.05, 0.1) with BZCYYb; (d) $LSFNM_x$ ($x$=0, 0.05, 0.1) in Ar−21%$O_2$ (3% $H_2O$) atmosphere

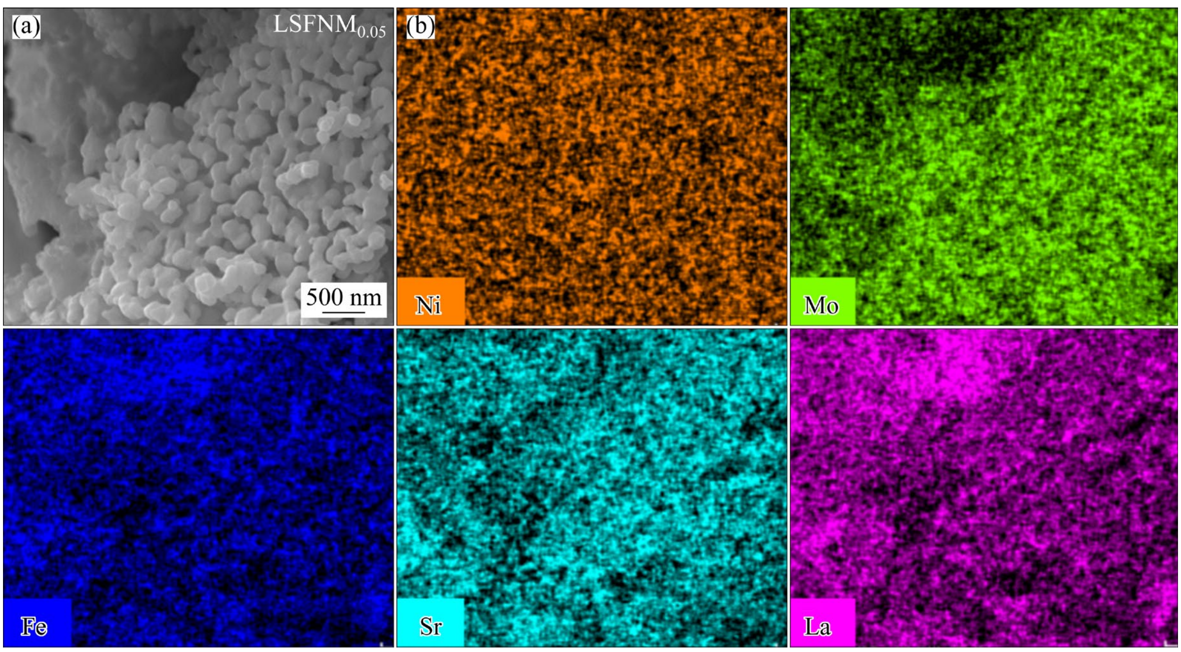


**Fig. 2** SEM image (a) and EDS elemental mappings (b) of $LSFNM_{0.05}$

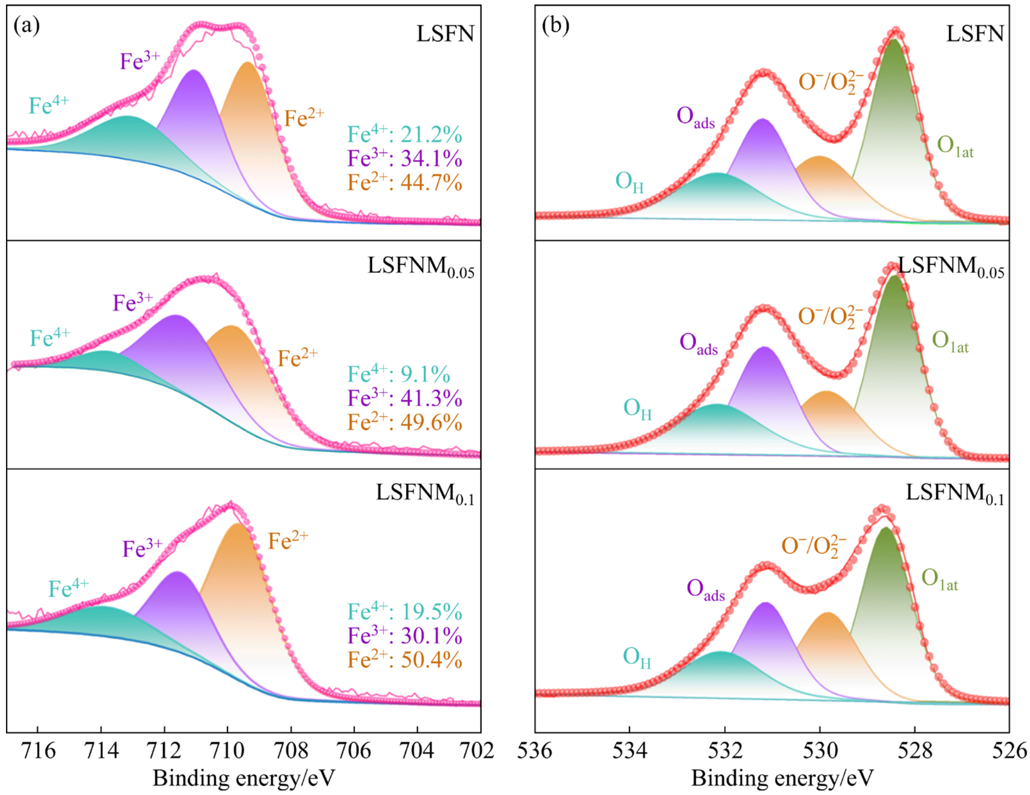


**Fig. 3** XPS spectra of Fe $2p_{3/2}$ (a) and O 1s (b)

LSFNM$_x$ ($x$=0, 0.05, 0.1). The proportions of Fe at different oxidation states were determined by analyzing the peak areas. In the Fe $2p_{3/2}$ spectrum, peaks at approximately 709, 711, and 713 eV correspond to $Fe^{2+}$, $Fe^{3+}$, and $Fe^{4+}$, respectively [22]. The proportions of $Fe^{4+}$ for LSFN, LSFNM$_{0.05}$, and LSFNM$_{0.1}$ were 21.2%, 9.1%, and 19.5%, respectively. Since Fe content significantly exceeds that of Ni and Mo, many high-spin $Fe^{4+}/Fe^{3+}$ reduction electron pairs are present [23]. Upon Mo doping, a portion of $Fe^{4+}$ is replaced by $Mo^{6+}$. Considering the charge valence state compensation mechanism, this substitution leads to a decrease in the proportion of $Fe^{4+}$, accompanied by an increase in the proportions of $Fe^{2+}$ and $Fe^{3+}$ [24]. According to Pauling's rule [25], the introduction of $Mo^{6+}$ as a positive ion reduces the connectivity of the common surface, resulting in fewer Fe—O bonds and, consequently, an increase in oxygen vacancies.

The generation of oxygen vacancies during the Mo doping process, which occurs to balance the decrease in the Fe valence state, can be analyzed through O 1s XPS spectra (Fig. 3(b)). The peaks with binding energies of 528−533 eV can be associated with the oxygen bonded to lattice oxygen ($O_{lat}$), $O^-/O^{2-}$, surface-adsorbed oxygen ($O_{ads}$), and structural water ($O_H$), respectively [26]. The $O^-/O^{2-}$ species indirectly reflect the concentration of oxygen vacancies ($O_{vac}$) [27]. These concentrations are quantified by calculating the ratio of each peak area to the total peak area [27,28]. As shown in Table 1, the oxygen vacancy concentration of LSFN, LSFNM$_{0.05}$, and LSFNM$_{0.1}$ is 20.12%, 24.00%, and 23.03%, respectively. Compared to that of LSFN, the oxygen vacancy concentration increases by 3.88% for LSFNM$_{0.05}$ and 2.91% for LSFNM$_{0.1}$. The results indicate that increasing Mo doping does not yield better outcomes, precisely because when Mo is doped too much, it replaces more $Fe^{4+}$ and leads to more lattice oxygen loss, which can be obtained by [29−31]

$$2Fe^{4+}+O_O^{\times} \rightarrow 2Fe^{3+}+V_O^{\bullet\bullet} \tag{1}$$

where $O_O^{\times}$ represents lattice oxygen; $V_O^{\bullet\bullet}$ stands for oxygen vacancy.

The thermogravimetric analysis (TGA) was employed to investigate the oxygen release behavior of the materials during the heating process. Figure 4 presents the thermogravimetric curves for the three materials heated from 30 to 900 °C in air. All three materials exhibit continuous mass loss with increasing temperature, primarily attributed to

**Table 1** Fitting results of O 1s XPS peaks of $LSFNM_x$ ($x$=0, 0.05, 0.1) samples

| Sample | Relative peak area | | | | Proporiton of $O_{vac}$/% |
|---|---|---|---|---|---|
| | $O_{lat}$ | $O^-/O^{2-}$ | $O_{ads}$ | $O_H$ | |
| LSFN | 61101.77 | 29873.05 | 33855.05 | 23639.40 | 20.12 |
| $LSFNM_{0.05}$ | 87369.17 | 46790.67 | 29221.22 | 32012.27 | 24.00 |
| $LSFNM_{0.1}$ | 84938.84 | 49717.77 | 48806.30 | 32408.11 | 23.03 |

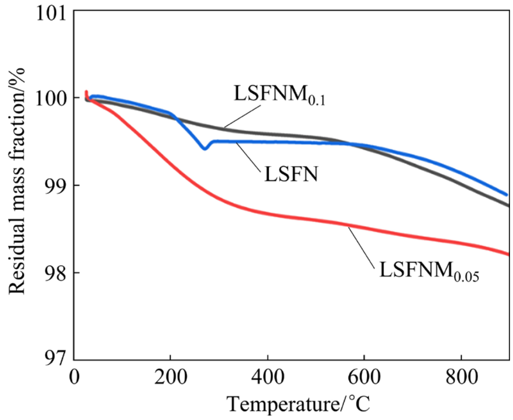


**Fig. 4** TGA curves of $LSFNM_x$ ($x$=0, 0.05, 0.1) at 30−900 °C in air

the loss of lattice oxygen. In the lower temperature range of 100−300 °C, the observed mass loss is predominantly due to the desorption of physically adsorbed surface water. As the temperature rises, further mass loss occurs, which can be attributed to the release of lattice oxygen [32]. The total mass loss values for LSFN, $LSFNM_{0.05}$, and $LSFNM_{0.1}$ are 1.11%, 2.1%, and 1.5%, respectively. Notably, $LSFNM_{0.05}$ demonstrates the highest oxygen loss value, indicating that lattice oxygen is more readily released during the heating process, generating a more significant number of oxygen vacancies. This observation is consistent with the XPS results previously discussed.

### 3.3 Electrical conductivity

As shown in Figs. 5(a) and (b), the conductivity curves for 5% and 10% Mo-doped samples exhibit similar trends under two atmospheres. At lower temperatures, the conductivity increases with rising temperature, primarily due to the thermal activation of small polaron conduction mechanisms [30]. The conductivity reaches its peak value at 650 °C, which is consistent with the conductive characteristics of p-type semiconductors. p-type carriers are mainly provided by the $Fe^{4+}$ charge compensating associated electron−hole pairs. The carrier concentration decreases with the thermal reduction of B-site cations and the intensification of lattice oxygen release at high temperatures. The relationship between lattice oxygen $O_O^\times$, oxygen vacancy $V_O^{\bullet\bullet}$, and electron−hole pairs ($h^\bullet$) is shown in Eq. (2). At elevated temperatures, the exacerbated loss of lattice oxygen results in increased oxygen vacancies and a corresponding decrease in electron−hole pairs. This process ultimately leads to a reduction in conductivity.

$$O_O^\times + 2h^\bullet \rightarrow \frac{1}{2}O_2 + V_O^{\bullet\bullet} \tag{2}$$

Upon Mo doping, LSFN exhibits the highest conductivity characteristics across both atmospheric conditions, while $LSFNM_{0.1}$ demonstrates the lowest conductivity. This phenomenon can be attributed to the introduction of high-valence Mo states, which trigger a partial conversion of $Fe^{4+}$ to $Fe^{3+}$ to maintain charge balance within the perovskite structure. This conversion results in a reduction of charge carriers, ultimately affecting the material's overall conductivity. However, the presence of $Mo^{6+}$ and $Mo^{5+}$ redox electron pairs can effectively overlap with $Fe^{3+}$ and $Fe^{2+}$ pairs, thereby ensuring the stability of the material's structure. Previous research [33] showed that Mo-doped LSFN, when used as an electrode material, demonstrated excellent stability in long-term testing (100 h), suggesting that Mo-doping can significantly enhance the structural stability of the battery. The conductivity of the material is slightly higher in an atmosphere containing $H_2O$. The increase in conductivity in moist air is due to proton conduction. Therefore, LSF-based materials meet the requirements of positive electrode operation of fuel cells [34].

Figures 5(c) and (d) show the Arrhenius diagrams corresponding to the conductivity of the three materials in different atmospheres and the magnitude of the activation energy. The activation energy can be calculated by the following equation:

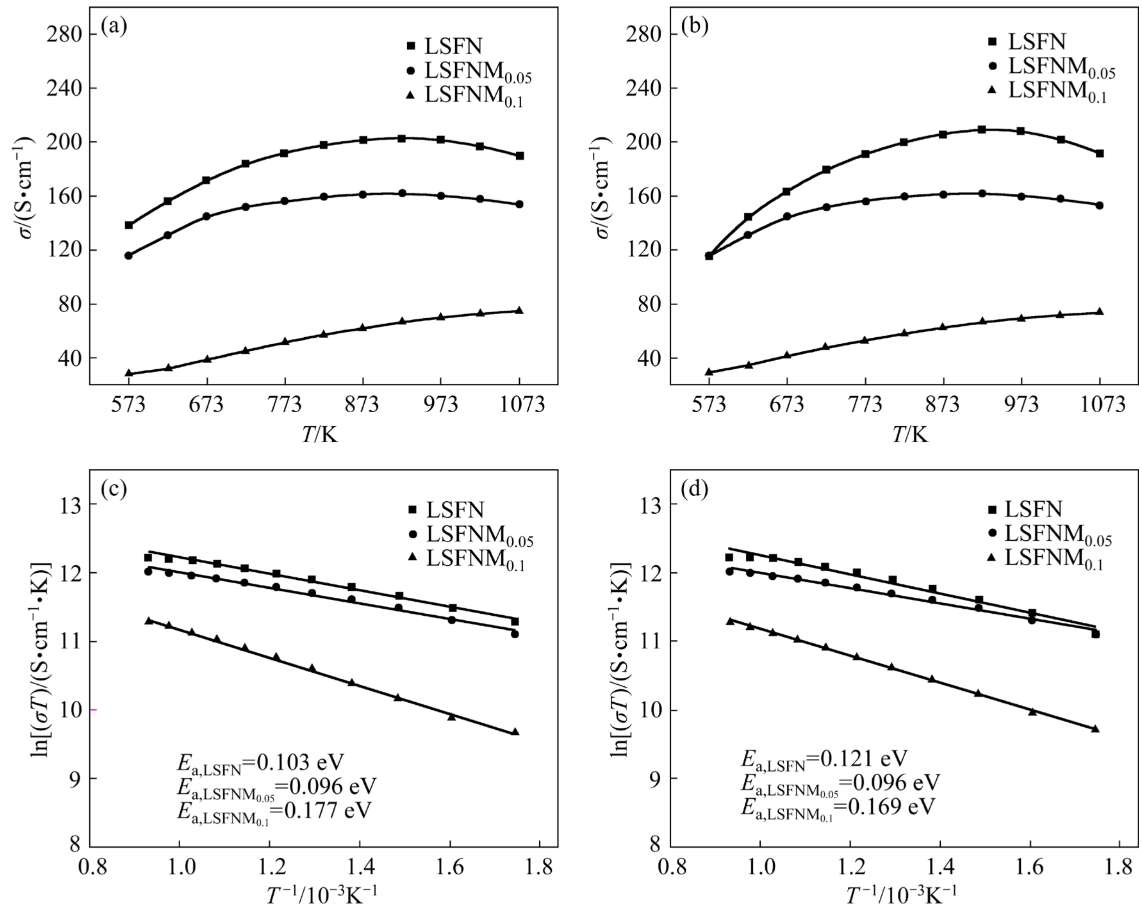


**Fig. 5** Conductivity curves (a, b) and corresponding Arrhenius plots (c, d) of $LSFNM_x$ ($x$=0, 0.05, 0.1) in different atmospheres: (a, c) Air; (b, d) Wet air

$$\sigma=\frac{A}{T}\exp\left(\frac{-E_a}{RT}\right) \tag{3}$$

where $\sigma$ is the electrical conductivity in S/cm; $A$ is the pre-exponential factor; $E_a$ is the activation energy in eV; $T$ is the thermodynamic temperature in K; $R$ is the molar gas constant (8.314 J/(mol·K)).

The $E_a$ value corresponds to the activation energy in a substance. The activation energies $E_a$ of $LSFNM_x$ ($x$=0, 0.05, 0.1) in air were 0.103, 0.096, and 0.177 eV, respectively. The activation energies under wet air conditions were 0.121, 0.096, and 0.169 eV, respectively. This shows that the electronic transition of LSFN material is more likely to occur under air conditions. When doped with Mo, its activation energy does not change under any atmosphere conditions. The minimal activation energy exhibited by $LSFNM_{0.05}$ signifies an enhanced capacity for electronic transitions. This characteristic is particularly desirable for cathode materials in H-SOFCs, as it can facilitate more efficient electrochemical processes.

### 3.4 Cell performance and stability

To study the ORR of the LSFN, $LSFNM_{0.05}$, and $LSFNM_{0.1}$ electrodes, the surface-specific resistance (ASR) of the symmetric battery under air condition was tested. The results of these tests are presented in Fig. 6. Due to the symmetry of the half-cell structure, the polarization resistance value in the ASR is divided by 2 to obtain the polarization resistance $R_{pol}$ of a single electrode. At 700 °C, the $LSFNM_{0.05}$ has a minimum $R_{pol}$ of 0.16 Ω·cm$^2$ in the three symmetric batteries, indicating that ORR can be effectively improved with doping 5% Mo as the cathode.

Figures 7(a−c) show the $J$−$V$−$P$ ($P$ is the power density) curves of IT-SOFC with LSFN and $LSFNM_x$ ($x$=0.05, 0.1) as cathodes, respectively. At 700, 650, 600, and 550 °C, the maximum power density of the battery with $LSFNM_{0.05}$ as the cathode is 484, 300, 172, and 106 mW/cm$^2$, respectively. The maximum power density of the battery with $LSFNM_{0.1}$ as the cathode is 365, 270, 170, 98 mW/cm$^2$, and the maximum power density

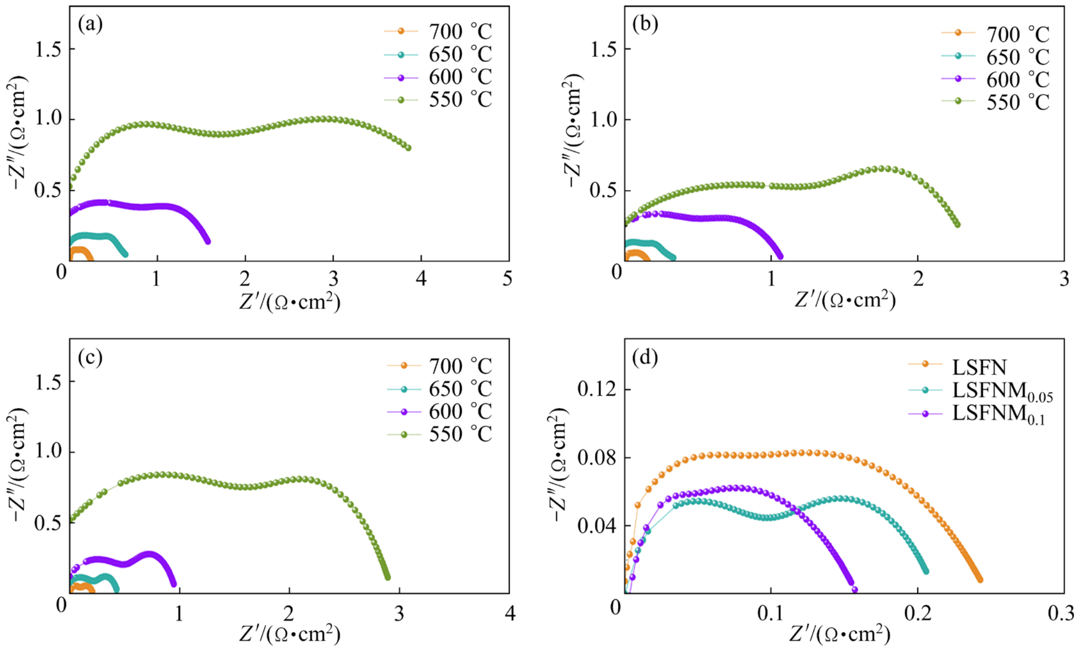

**Fig. 6** EIS results of symmetric cells: (a) LSFN; (b) $LSFNM_{0.05}$; (c) $LSFNM_{0.1}$; (d) Symmetric cells at 700 °C under air conditions

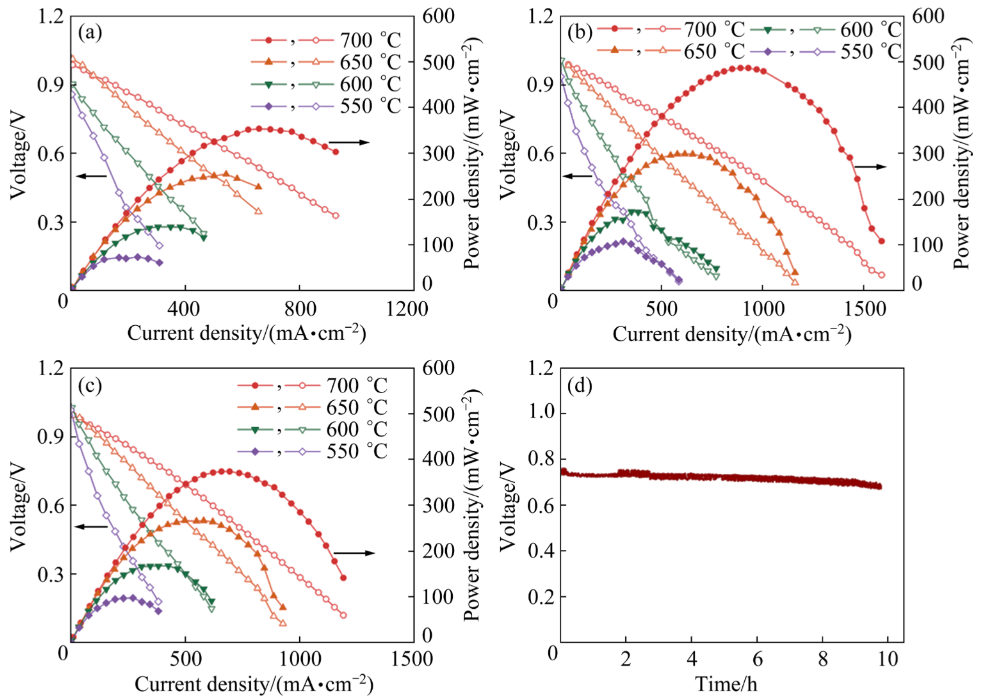

**Fig. 7** *J*−*V*−*P* curves for single cell using LSFN (a), $LSFNM_{0.05}$ (b) and $LSFNM_{0.1}$ (c) cathodes, and output stability of single cell with $LSFNM_{0.05}$ as cathode at 550 mA/cm$^2$ and 700 °C (d)

of the battery with LSFN as the cathode is 353, 253, 141, and 75 mW/cm$^2$ at the same temperature, respectively. Compared with undoped LSFN, the power density is improved to a certain extent. This indicates that Mo doping is conducive to improving the catalytic activity of LSFN cathode materials. Figure 7(d) illustrates the output stability of a single cell employing $LSFNM_{0.05}$ as the cathode at 700 °C. The cell, with an effective area of 0.26 cm$^2$, was operated at a constant current density of 550 mA/cm$^2$. During the test, the cell output voltage exhibited a decay rate of 0.6%/h.

As shown in Figs. 8(a) and (b), the cross-sectional microstructure of the anode and cathode are observed by scanning electron microscope. The thickness of the electrolyte and cathode is 20−30 μm, the thickness of the anode is about 500 μm, and the electrodes are in good contact with the electrolyte, which proves that they have good chemical compatibility with the electrolyte and ensure the long-term work of the battery.

Figure 9 shows the EIS spectra of H-SOFC with LSFN, $LSFNM_{0.05}$, and $LSFNM_{0.1}$ as cathodes at open circuit voltage, respectively. The impedance

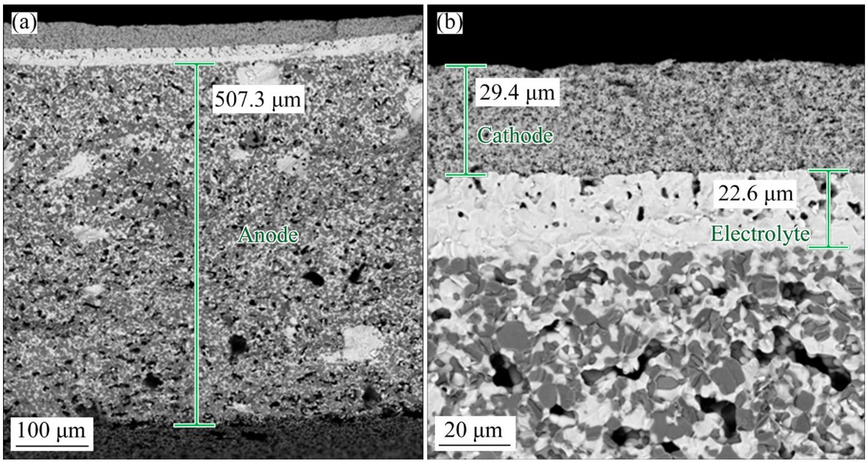


**Fig. 8** SEM images of cross-section of anode (a) and cathode (b) after stability test

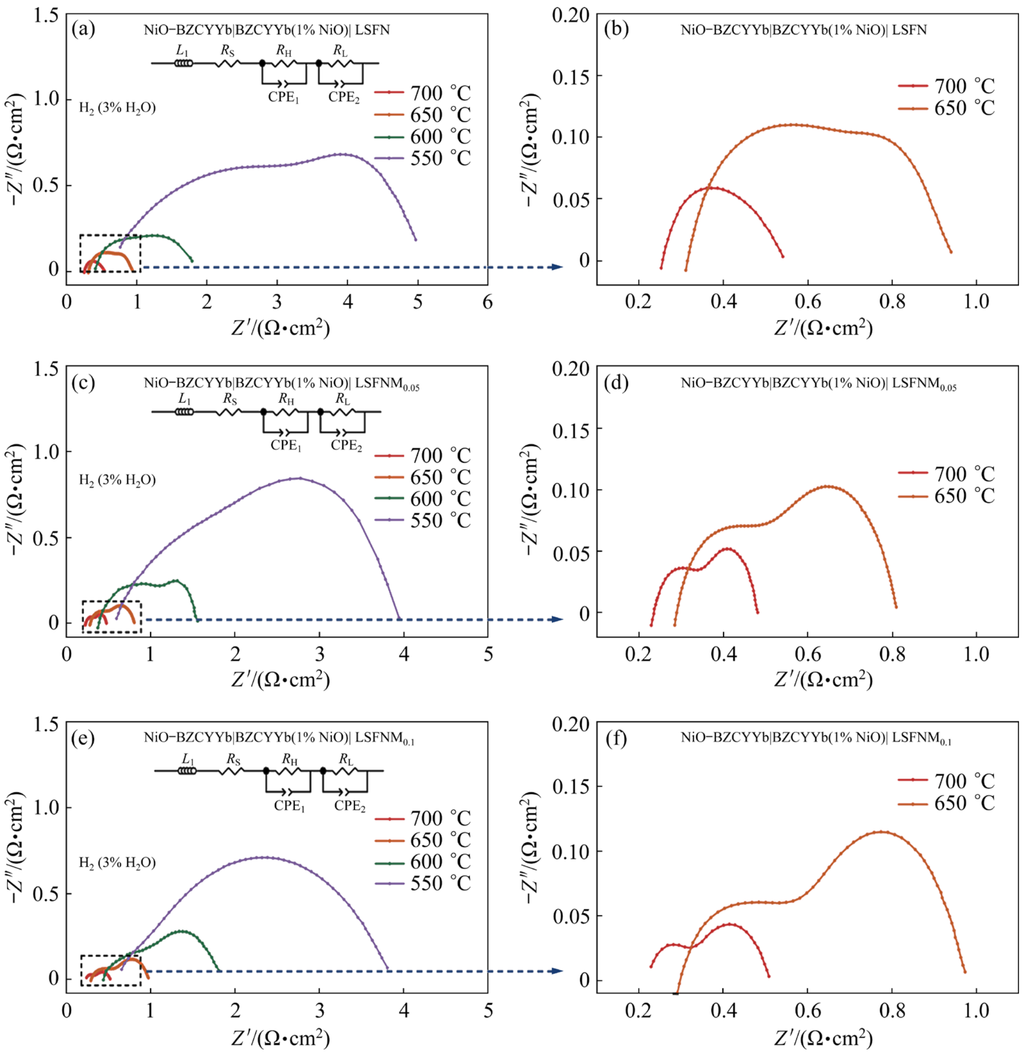


**Fig. 9** EIS spectra of single cells at different temperatures: (a, b) LSFN; (c, d) $LSFNM_{0.05}$; (e, f) $LSFNM_{0.1}$

spectrum mainly consists of ohm resistance ($R_{\Omega}$) and polarization resistance $R_{pol}$. The horizontal coordinate of the starting point of the spectrum in Fig. 9 represents the ohmic resistance of the battery, which is mainly affected by the electrolyte. The difference between the horizontal coordinate of the endpoint and the starting point can be approximately understood as the polarization resistance of the fuel cell. It can be seen from Fig. 9 that the $R_{pol}$ of these three cathode materials decreases with the increase in temperature, which indicates that LSF-based materials can maintain good stability and electrochemical activity under high temperature. As shown in Fig. 9, the polarization resistance $R_{pol}$ for LSFN, $LSFNM_{0.05}$, and $LSFNM_{0.1}$ at 700 °C is 0.30, 0.26, and 0.27 $\Omega\cdot cm^2$, respectively. In contrast, the $R_{pol}$ value of the cathode material $LSFNM_{0.05}$ at 700 °C is lower than that of most LSFN cathode materials [35]. The polarization resistance of the electrode is mainly composed of the polarization resistance of the cathode, indicating that the Mo- doped cathode exhibits good ORR activity. At 700 °C, the $R_{pol}$ is only 0.26 $\Omega\cdot cm^2$. The spray coating method can simultaneously ensure low ohmic resistance and high electrolyte material density, thus enhancing the chemical performance of the battery.

### 3.5 DRT analysis results

To effectively distinguish these electrochemical steps, the EIS spectra are analyzed using the DRT method [36,37]. The EIS data were analyzed based on the DRT results in Fig. 10. Each peak in the diagram represents a specific reaction step in the fuel cell reaction process. The peak areas reflect the contribution of each step to the overall polarization resistance, allowing identification of the rate-limiting step in the reaction. We label the peaks that occur with temperature as P1−P5 in the frequency order from high to low. Combined with the current DRT analysis of proton conduction solid oxide fuel cells and the results of literature, the corresponding DRT peaks in this work are listed in Table 2 [38,39].

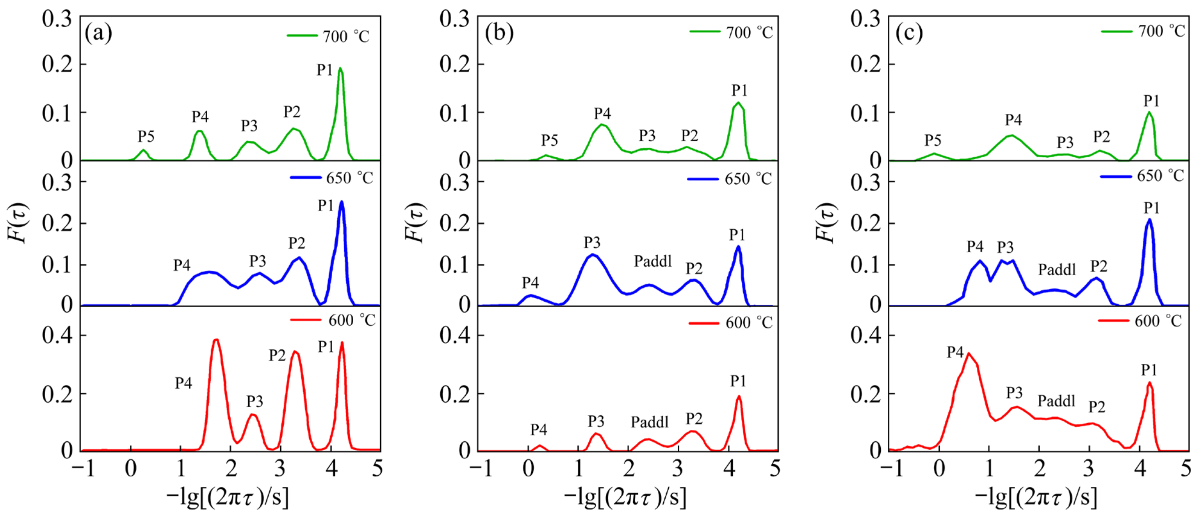


**Fig. 10** DRT diagrams of H-SOFC with LSFN (a), $LSFNM_{0.05}$ (b), $LSFNM_{0.1}$ (c) as cathodes at 700 °C ($\tau$ is relaxation time)

**Table 2** Reaction steps corresponding to different peaks in fitting process [38,39]

| Peak | Reaction process |
|---|---|
| P1 | Proton diffusion; A lattice of protons bound to an anode [38] |
| P2 | Hydrogen adsorption and dissociation; Proton forming [38] |
| P3 | Oxygen reduction process [38] |
| P4 | Oxygen adsorption and dissociation; Oxygen diffusion [38] |
| P5 | Diffusion of anodes in porous gases [38] |
| Padd1 | Oxygen binds to the lattice [39] |

The intensity of the peak increases as the temperature decreases, indicating a slower reaction rate at lower temperatures. Peak P5 begins to disappear for all single cells at 650 °C, indicating that the reaction step corresponding to P5 is not a rate-limiting step at low temperatures (Fig. 10). Additionally, as the temperature decreases, a new peak (Padd1) appears between P2 and P3, which means that some non-rate-limiting processes become rate-limited. Due to the cell's anode-supported structure, the area of peak P1 is relatively large, which can be attributed to the greater thickness of the anode.

Generally, the peaks associated with cathode reactions (Padd1, P3, and P4) predominate within all test temperature ranges, which implies that the cathode is the most significant source of $R_{pol}$. Figures 10(b) and (c) show that the ordinate height of $LSFNM_x$ at the same temperature, by contrast, is significantly lower than that of LSFN, which also corresponds to the $R_{pol}$ with the smaller single cell in the front. Mo-doped LSFN enhances the oxygen ion migration capacity of the cathode, and the $LSFNM_x$ cathode shows better performance. Therefore, enhancing oxygen ion migration is an effective way to reduce significant oxygen polarization in H-SOFC.

The sum of the area of Peaks P1−P5 represents the polarization resistance of the entire single cell. As the temperature decreases, the polarization resistance increases correspondingly. The polarization resistance of $LSFNM_{0.05}$ is minimal at 700 °C, which ensures good battery performance. The data also reveal that, after Mo doping, the peaks associated with the cathode reaction (Padd1, P3, and P4) dominate the temperature range. As shown in Fig. 11, Peaks P3 and P4, observed at 600−700 °C, represent the primary limiting factors. At 700 °C, the polarization resistance of $LSFNM_{0.05}$ is minimized, with oxygen adsorption and desorption as the key components of the process. However, this process positively correlates with the oxygen vacancy concentration discussed above. The XPS results show that the oxygen vacancy concentration of $LSFNM_{0.05}$ is the highest. So, the results are consistent. Mo doping is beneficial to the optimization related to oxygen cathode behavior, which provides a new direction for research on the mechanism of H-SOFC.

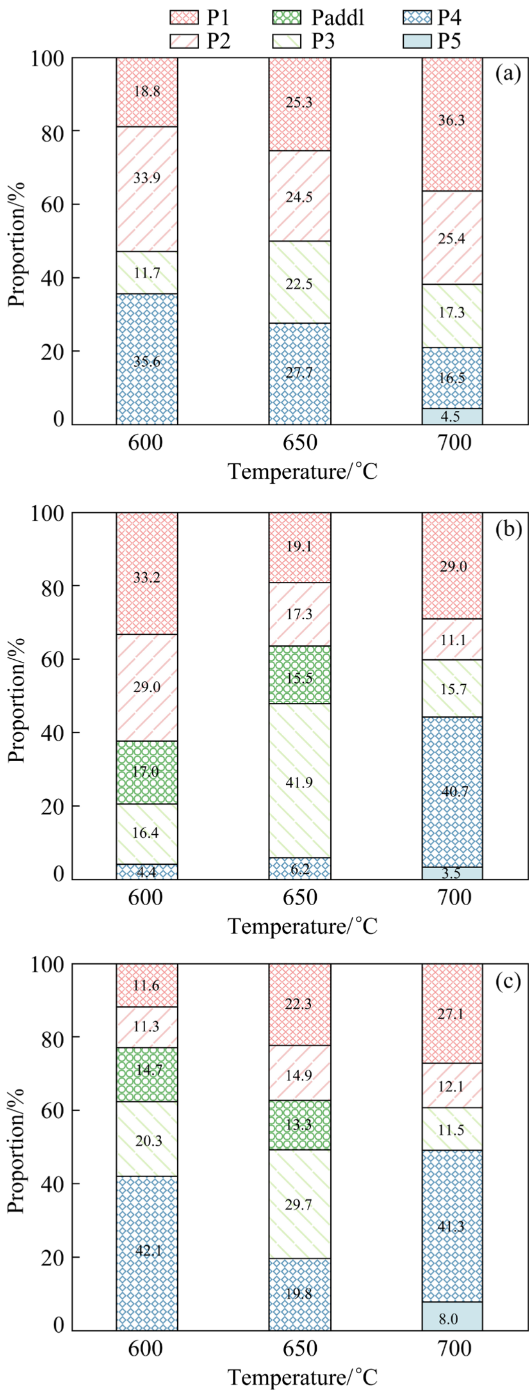


**Fig. 11** Proportions of individual polarization resistance processes of three different cathodes at different temperatures: (a) LSFN; (b) $LSFNM_{0.05}$; (c) $LSFNM_{0.1}$

It can be seen from Table 3 that the power density and polarization resistance of $LSFNM_{0.05}$ cathode materials are 484 mW/cm$^2$ and 0.26 Ω·cm$^2$, respectively. Compared with that of the undoped LSFN, the power density increases by 37%, and the polarization resistance decreases by 13%. This shows that Mo doping improves the electrocatalytic

**Table 3** Power density and polarization resistance of perovskite material used as cathode of fuel electrode

| Cathode material | Power density/ (mW·cm$^{-2}$) | Polarization resistance/ (Ω·cm$^2$) | Temperature/ °C | Source |
|---|---|---|---|---|
| $La_{0.8}Sr_{0.2}Fe_{0.7}Ni_{0.3}$-GDC | 500 | | 700 | [40] |
| $(La_{0.6}Sr_{0.4})_{0.9}Fe_{0.8}Ni_{0.2}O_{3-\delta}$ | 630 | 0.078 | 700 | [41] |
| $La_{0.7}Sr_{0.3}FeO_{3-\delta}$-SDC | 542 | 0.074 | 650 | [42] |
| $La_{0.25}Sr_{2.75}FeNiO_{3-\delta}BaZr_{0.1}Ce_{0.7}Y_{0.2}O_{3-\delta}$ | 426 | 0.26 | 650 | [43] |
| $La_{0.6}Sr_{0.3}Ce_{0.1}Fe_{0.9}Ni_{0.1}O_{3-\delta}$ | 725 | 0.13 | 700 | [44] |
| $La_{0.5}Sr_{0.5}FeO_{3-\delta}$ | | 0.79 | 700 | [45] |
| $SrFe_{0.9}Nb_{0.1}O_{3-\delta}$ | | 0.29 | 700 | [46] |
| $Sr_{0.95}Ce_{0.05}CoO_{3-\delta}$-GDC | 546 | 0.152 | 650 | [47] |
| $La_{0.6}Sr_{0.4}Fe_{0.9}Ni_{0.1}O_{3-\delta}$ | 405 | 0.14 | 700 | [18] |
| $La_{0.6}Sr_{0.4}Fe_{0.85}Ni_{0.1}Mo_{0.05}$ | 484 | 0.26 | 700 | This work |

activity and stability of the electrode material [35]. It is beneficial to the progress of ORR and consistent with the results of the XPS analysis mentioned above. Mo doping is an effective way to improve the properties of perovskite structural materials, and the catalytic activity and stability of positive electrode materials. Compared with that of some LSFN composites (i.e. $La_{0.8}Sr_{0.2}Fe_{0.7}Ni_{0.3}$-GDC) [40] or LSFN cathode materials with A-position defects ($(La_{0.6}Sr_{0.4})_{0.9}Fe_{0.8}Ni_{0.2}O_{3-\delta}$) [41], the performance of $LSFNM_{0.05}$ in this work is slightly worse. This is related to the electrolyte conducting different ions. In summary, Mo doping improves the electrochemical properties of LSFN cathode materials to a certain extent. The introduction of Mo can also increase the oxygen vacancy concentration and ORR capacity of $LSFNM_{0.05}$, which is conducive to the ORR in the cathode.

## 4 Conclusions

(1) The perovskite materials with different proportions of Mo-doped $LSFNM_x$ ($x$=0.05, 0.1) have a pure phase structure. When simulating the fuel cell cathode, it maintains stability and has good chemical compatibility under different operating conditions.

(2) From the chemical state of O in the XPS results, the doping of Mo increases the oxygen vacancy concentration and accelerates proton transportation. Compared with LSFN (20.12%) and $LSFNM_{0.1}$ (23.03%), $LSFNM_{0.05}$ reaches the maximum oxygen vacancy concentration (24.00%).

(3) Although Mo doping reduces the conductivity of the material to a certain extent, $LSFNM_x$ can still meet the requirements of fuel cell cathode materials due to the conductivity of the high activity of Ni.

(4) The electrochemical test results of the single cell show that the $LSFNM_{0.05}$ as the cathode has the lowest polarization resistance of 0.26 Ω·cm$^2$ and the highest power density of 484 mW/cm$^2$ at 700 °C.

### CRediT authorship contribution statement

**Ting TING:** Visualization, Data curation, Conceptualization; Writing − Original draft, Writing − Review & editing; **Di XIE:** Formal analysis, Writing − Original draft; **Li CHEN:** Investigation, Formal analysis; **Li-jun WANG:** Methodology, Supervision, Resources, Funding acquisition.

### Declaration of competing interest

The authors declare that they have no known competing financial interests or personal relationships that could have appeared to influence the work reported in this paper.

### Acknowledgments

The authors are grateful for the financial support from the National Natural Science Foundation of China (Nos. 51922003, 52274406), and the Fundamental Research Funds for the Central Universities, China (No. FRF-BD-23-02).

## References


[1] AKSENOVA T V, MYSIK D K, CHEREPANOV V A. Crystal structure and properties of $Gd_{1-x}Sr_xCo_{1-y}Fe_yO_{3-\delta}$ oxides as promising materials for catalytic and SOFC application [J]. Catalysts, 2022, 12(11): 1344.

[2] ALIMI W, CHOUIKH R, GUIZANI A A. SOFC modelling considering radiation heat transfer [J]. Mechanics & Industry, 2020, 21(3): 306.

[3] ASCOLANI-YAEL J, MONTENEGRO-HERNÁNDEZ A, LIU Q, BARNETT S A, MOGNI L. Study of $La_{0.6}Sr_{0.4}$-$Co_{1-x}Fe_xO_{3-\delta}$ ($x$=0.2 & 0.8) electrochemical response as SOFC cathodes and its relation with microstructure [J]. Journal of the Electrochemical Society, 2019, 166(16): F1301−F1307.

[4] CAO Y, TOWHID P. A solar-driven lumped SOFC/SOEC system for electricity and hydrogen production: 3E analyses and a comparison of different multi-objective optimization algorithms [J]. Journal of Cleaner Production, 2020, 271: 122457.

[5] MEDVEDEV D A, LYAGAEVA J G, GORBOVA E V, DEMIN A K, TSIAKARAS P. Advanced materials for SOFC application: Strategies for the development of highly conductive and stable solid oxide proton electrolytes [J]. Progress in Materials Science, 2016, 75: 38−79.

[6] AHUJA A, GAUTAM M, SINHA A, SHARMA J, PATRO P K, VENKATASUBRAMANIAN A. Effect of processing route on the properties of LSCF-based composite cathode for IT-SOFC [J]. Bulletin of Materials Science, 2020, 43(1): 1−9.

[7] ALIZADEH S M, MOHEBBI H, GOLMOHAMMAD M, SHARIFI O, FARZANEH F. Revisiting Fe-doped 8YSZ as the electrolyte of SOFC—From sintering to electrochemical performance [J]. Journal of Alloys and Compounds, 2023, 938: 168553.

[8] CAVALLI A, CHUNDRU P, BRUNNER T, OBERNBERGER I, MIRABELLI I, MAKKUS R, ARAVIND P V. Interactions of high temperature $H_2S$ and HCl cleaning sorbents with biosyngas main components and testing in a pilot integrated biomass gasifier SOFC system [J]. Renewable Energy, 2021, 180: 673−682.

[9] HOU Jie, YANG Guang-hui, LIU Wei. The principles for rationally designing H-SOFC anode active layer [J]. Materials Research Bulletin, 2022, 150: 111769.

[10] KALPANA DEVI A, RAM KUMAR G, PRERNA C, AMARSINGH BHABU K, SABARINATHAN V, RAJASEKARAN T R. Superionic conductive $La^{3+}$ and $Pr^{3+}$ Co-doped cerium oxide for IT-SOFC applications [J]. Journal of Materials Science: Materials in Electronics, 2020, 31(13): 10628−10638.

[11] LU Fei, YANG Meng-jie, SHI Yun-jia, WU Chang-hui, JIA Xu-sheng, HE Hao, SU Jin-rui, CHAO Ming-ju, CAI Bin. Application of a negative thermal expansion oxide in SOFC cathode [J]. Ceramics International, 2021, 47(1): 1095−1100.

[12] CHEN Li, HOU Yun-ting, ZHANG Qi-fei, WANG Li-jun, ZHOU Guo-zhi. Research progress of proton-conducting solid oxide fuel cell materials and electrochemical performance [J]. The Chinese Journal of Nonferrous Metals, 2021, 31(11): 3217−3231. (in Chinese)

[13] KASYANOVA A V, ZVONAREVA I A, TARASOVA N A, BI Lei, MEDVEDEV D A, SHAO Zong-ping. Electrolyte materials for protonic ceramic electrochemical cells: Main limitations and potential solutions [J]. Materials Reports: Energy, 2022, 2(4): 100158.

[14] LIU Zuo-qing, TANG Zheng-jie, SONG Yu-fei, YANG Guang-ming, QIAN Wan-ru, YANG Mei-ting, ZHU Yin-long, RAN Ran, WANG Wei, ZHOU Wei, SHAO Zong-ping. High-entropy perovskite oxide: A new opportunity for developing highly active and durable air electrode for reversible protonic ceramic electrochemical cells [J]. Nano-Micro Letters, 2022, 14(1): 217.

[15] KALPANA DEVI A, RAM KUMAR G, PRERNA C, AMARSINGH BHABU K, DANIEL C, SABARINATHAN V, RAJASEKARAN T R. Investigations on positive ($Sm^{3+}$) and negative ($Ho^{3+}$) association energy ion Co-doped cerium oxide solid electrolytes for IT-SOFC applications [J]. JOM, 2021, 73(9): 2754−2763.

[16] DHONGDE V, SINGH A, KALA J, ANJUM U, HAIDER M A, BASU S. Radio-frequency magnetron sputtered thin-film $La_{0.5}Sr_{0.5}Co_{0.95}Nb_{0.05}O_{3-\delta}$ perovskite electrodes for intermediate temperature symmetric solid oxide fuel cell (IT-SSOFC) [J]. Materials Reports: Energy, 2022, 2(2): 100095.

[17] ZOU Dan, YI Yong-ning, SONG Yu-fei, GUAN Da-qin, XU Mei-gui, RAN Ran, WANG Wei, ZHOU Wei, SHAO Zong-ping. The $BaCe_{0.16}Y_{0.04}Fe_{0.8}O_{3-\delta}$ nanocomposite: A new high-performance cobalt-free triple-conducting cathode for protonic ceramic fuel cells operating at reduced temperatures [J]. Journal of Materials Chemistry A, 2022, 10(10): 5381−5390.

[18] ZHANG F, YANG Z, WANG H, WANG W, MA G. Performance of cobalt-free $La_{0.6}Sr_{0.4}Fe_{0.9}Ni_{0.1}O_{3-\delta}$ cathode material for intermediate temperature solid oxide [J]. Fuel Cells, 2012, 12(5): 749−753.

[19] LU Xiao-yong, YANG Yang, DING Yan-zhi, CHEN Yong-hong, GU Qing-wen, TIAN Dong, YU Wei-li, LIN Bin. Mo-doped $Pr_{0.6}Sr_{0.4}Fe_{0.8}Ni_{0.2}O_{3-\delta}$ as potential electrodes for intermediate-temperature symmetrical solid oxide fuel cells [J]. Electrochimica Acta, 2017, 227: 33−40.

[20] ZHANG Qi-fei, HOU Yun-ting, CHEN Li, WANG Li-jun, CHOU K C. Enhancement of electrochemical performance for proton conductive solid oxide fuel cell by 30%GDC−LSCF cathode [J]. Ceramics International, 2022, 48(12): 17816−17827.

[21] BEN MYA O, DOS SANTOS-GÓMEZ L, PORRAS-VÁZQUEZ J M, OMARI M, RAMOS-BARRADO J R, MARRERO-LÓPEZ D. $La_{1-x}Sr_xFe_{0.7}Ni_{0.3}O_{3-\delta}$ as both cathode and anode materials for solid oxide fuel cells [J]. International Journal of Hydrogen Energy, 2017, 42(36): 23160−23169.

[22] LIU Bo, YANG Jia-jun, YAN Dong, JIA Li-chao, CHI Bo, PU Jian, LI Jian. Novel $PrBa_{0.9}Ca_{0.1}CO_{2-x}Zn_xO_{5+\delta}$ double-perovskite as an active cathode material for high-performance proton-conducting solid oxide fuel cells [J]. International Journal of Hydrogen Energy, 2020, 45(55):

31009−31016.

[23] XU Xi, XU Yang-sen, MA Jin-ming, YIN Yan-ru, FRONZI M, WANG Xian-fen, BI Lei. Tailoring electronic structure of perovskite cathode for proton-conducting solid oxide fuel cells with high performance [J]. Journal of Power Sources, 2021, 489: 229486.

[24] LV Xiu-qing, CHEN Hui-li, ZHOU Wei, CHENG Fang-qin, LI Si-dian, SHAO Zong-ping. Direct-methane solid oxide fuel cells with an in situ formed Ni−Fe alloy composite catalyst layer over Ni−YSZ anodes [J]. Renewable Energy, 2020, 150: 334−341.

[25] ZHANG Xiao-min, SONG Yue-feng, WANG Guo-xiong, BAO Xin-he. Co-electrolysis of $CO_2$ and $H_2O$ in high-temperature solid oxide electrolysis cells: Recent advance in cathodes [J]. Journal of Energy Chemistry, 2017, 26(5): 839−853.

[26] WANG Zhi-chao, XU Wen-jia, CHEN Xiao-kang, PENG Yan-hua, SONG Yan-yan, LV Chun-xiao, LIU Hong-li, SUN Jun-wei, YUAN Ding, LI Xi-yan, GUO Xiang-xin, YANG Dong-jiang, ZHANG Li-xue. Defect-rich nitrogen doped $Co_3O_4$/C porous nanocubes enable high-efficiency bifunctional oxygen electrocatalysis [J]. Advanced Functional Materials, 2019, 29(33): 1902875.

[27] JIA Wei-hua, HUANG Zhuo-nan, SUN Wen, WU Le, ZHENG Lan, WANG Yu-qi, HUANG Jian-bing, YANG Xin, LV Ming, GE Lei. Flexible A-site doping $La_{0.6-x}M_xSr_{0.4}Co_{0.2}Fe_{0.8}O_3$ (M=Ca, Ba, Bi; $x$=0, 0.1, 0.2) as novel cathode material for intermediate-temperature solid oxide fuel cells: A first-principles study and experimental exploration [J]. Journal of Power Sources, 2021, 490: 229564.

[28] ZHOU Jun-fu, YE Lin, HUANG Dao-feng, WANG Mei-yin, REN Yuan-hang, YUE Bin, HE He-yong. The synergy of modulated surface polarity and oxygen vacancy for $CO_2$ to methanol over $Zn^{(\delta-)}-Ti^{(\delta+)}O$ vacancy [J]. Journal of Energy Chemistry, 2021, 56: 449−454.

[29] FENG Jie, YANG Guo-quan, DAI Ning-ning, WANG Zhen-hua, SUN Wang, ROONEY D, QIAO Jin-shuo, SUN Ke-ning. Investigation into the effect of Fe-site substitution on the performance of $Sr_2Fe_{1.5}Mo_{0.5}O_{6-\delta}$ anodes for SOFCs [J]. Journal of Materials Chemistry A, 2014, 2(41): 17628−17634.

[30] LI Xiao-mei, LIU Yin-hua, LIU Wen-yun, WANG Chao, XU Xi, DAI Hai-lu, WANG Xian-fen, BI Lei. Mo-doping allows high performance for a perovskite cathode applied in proton-conducting solid oxide fuel cells [J]. Sustainable Energy & Fuels, 2021, 5(17): 4261−4267.

[31] XIE Dong, LI Kai, YANG Jun, YAN Dong, JIA Li-chao, CHI Bo, PU Jian, LI Jian. High-performance $La_{0.5}(Ba_{0.75}Ca_{0.25})_{0.5}$-$Co_{0.8}Fe_{0.2}O_{3-\delta}$ cathode for proton-conducting solid oxide fuel cells [J]. International Journal of Hydrogen Energy, 2021, 46(15): 10007−10014.

[32] LIU Su-biao, LIU Qing-xia, LUO Jing-li. The excellence of $La(Sr)Fe(Ni)O_3$ as an active and efficient cathode for direct $CO_2$ electrochemical reduction at elevated temperatures [J]. Journal of Materials Chemistry A, 2017, 5(6): 2673−2680.

[33] HOU Yun-ting, WANG Li-jun, BIAN Liu-zhen, CHEN Ning, CHOU K C. High performance of Mo-doped $La_{0.6}$-$Sr_{0.4}Fe_{0.9}Ni_{0.1}O_{3-\delta}$ perovskites as anode for solid oxide fuel cells [J]. Electrochimica Acta, 2018, 292: 540−545.

[34] RAGER J, ZIPPERLE M, SHARMA A, MACMANUS-DRISCOLL J L. Oxygen stoichiometry in $Sr_2FeMoO_6$, the determination of Fe and Mo valence states, and the chemical phase diagram of $SrO-Fe_3O_4-MoO_3$ [J]. Journal of the American Ceramic Society, 2004, 87(7): 1330−1335.

[35] FAN Li-jun, RAUTAMA E L, LINDEN J, SAINIO J, JIANG Hua, SORSA O, HAN Na-na, FLOXl C, ZHAO Yi-cheng, LI Yong-dan, KALLIO T. Two orders of magnitude enhancement in oxygen evolution reactivity of $La_{0.7}Sr_{0.3}$-$Fe_{1-x}Ni_xO_{3-\delta}$ by improving the electrical conductivity [J]. Nano Energy, 2022, 93: 106794.

[36] CHOI S M, AN H, YOON K J, KIM B K, LEE H W, SON J W, KIM H, SHIN D, JI H I, LEE J H. Electrochemical analysis of high-performance protonic ceramic fuel cells based on a columnar-structured thin electrolyte [J]. Applied Energy, 2019, 233: 29−36.

[37] SHI Nai, SU Feng, HUAN Dao-ming, XIE Yun, LIN Jie, TAN Wen-zhou, PENG Ran-ran, XIA Chang-rong, CHEN Chu-sheng, LU Ya-lin. Performance and DRT analysis of P-SOFCs fabricated using new phase inversion combined tape casting technology [J]. Journal of Materials Chemistry A, 2017, 5(37): 19664−19671.

[38] HONG J, BHARDWAJ A, BAE H, KIM I H, SONG S J. Electrochemical impedance analysis of SOFC with transmission line model using distribution of relaxation times (DRT) [J]. Journal of the Electrochemical Society, 2020, 167(11): 114504.

[39] CHEN Jun-yu, LI Jin, JIA Li-chao, MOUSSA I, CHI Bo, PU Jia, LI Jian. A novel layered perovskite $Nd(Ba_{0.4}Sr_{0.4}Ca_{0.2})$-$Co_{1.6}Fe_{0.4}O_{5+\delta}$ as cathode for proton-conducting solid oxide fuel cells [J]. Journal of Power Sources, 2019, 428: 13−19.

[40] SADYKOV V, MEZENTSEVA N, USOLTSEV V, SADOVASKAYA E, ISHCHENKO A, PAVLOVA S, BESPALKO Y, KHARLAMOVA T, ZEVAK E, SALANOV A, KRIEGER T. Solid oxide fuel cell composite cathodes based on perovskite and fluorite structures [J]. Journal of Power Sources, 2011, 196(17): 7104−7109.

[41] WANG Xiang, ZHANG Yu-xi, WANG Zhao-wen, WANG Hao-ran, YU Miao, CHEN Ming, YANG Zhi-bin. Enhanced oxygen reduction reaction activity and electrochemical performance of A-site deficient $(La_{0.6}Sr_{0.4})_{1-x}Fe_{0.8}Ni_{0.2}O_{3-\delta}$ cathode for solid oxide fuel cells [J]. Ceramics International, 2023, 49(19): 31569−31575.

[42] SUN Wen-ping, FANG Shu-min, YAN Lit-ao, LIU Wei. Proton-blocking composite cathode for proton-conducting solid oxide fuel cell [J]. Journal of the Electrochemical Society, 2011, 158(11): B1432−B1438.

[43] LING Yi-han, GUO Tian-ming, GUO Yang-yang, YANG Yang, TIAN Yun-feng, WANG Xin-xin, OU Xue-mei, FENG Pei-zhong. New two-layer Ruddlesden−Popper cathode materials for protonic ceramics fuel cells [J]. Journal of Advanced Ceramics, 2021, 10(5): 1052−1060.

[44] BIAN Liu-zhen, WANG Li-jun, CHEN Ning, LI Fu-shen, CHOU K C. Enhanced performance of $La_{0.7}Sr_{0.3}Fe_{0.9}Ni_{0.1}O_3$ cathode by partial substitution with Ce [J]. Ceramics International, 2017, 43(1): 982−987.

[45] NIU Ying-jie, SUNARSO J, LIANG Feng-li, ZHOU Wei, ZHU Zhong-hua, SHAO Zong-ping. A comparative study of oxygen reduction reaction on Bi- and La-doped $SrFeO_{3-\delta}$ perovskite cathodes [J]. Journal of the Electrochemical Society, 2011, 158(2): B132−B138.

[46] ZHOU Qing-jun, ZHANG Lei-lei, HE Tian-min. Cobalt-free cathode material $SrFe_{0.9}Nb_{0.1}O_{3-\delta}$ for intermediate-temperature solid oxide fuel cells [J]. Electrochemistry Communications, 2010, 12(2): 285−287.

[47] LI Shu-ting, LIU Yuan-yuan, CAI Chang-kun, XUE Ke, BIAN Liu-zhen, AN Sheng-li. Ce-doped promotes the phase stability and electrochemical performance of $SrCoO_{3-\delta}$ cathode for intermediate-temperature solid oxide fuel cells [J]. Journal of Power Sources, 2024, 592: 233932.

# B 位 Mo 掺杂对 $La_{0.6}Sr_{0.4}Fe_{0.9}Ni_{0.1}O_{3-\delta}$ 质子传导型固体氧化物燃料电池正极材料电化学性能的影响

婷 婷，谢 帝，陈 力，王丽君

北京科技大学 钢铁技术协同创新中心，北京 100083

**摘 要**：为解决质子传导型固体氧化物燃料电池(H-SOFC)中氧空位不足的问题，在铁酸镧钙钛矿($ABO_3$)的 B 位引入过渡金属元素，进一步增强其催化活性。采用溶胶−凝胶法制备了 Mo 掺杂的 $La_{0.6}Sr_{0.4}Fe_{0.9-x}Ni_{0.1}Mo_xO_{3-\delta}$ (LSFNM$_x$, $x$=0.05, 0.1) H-SOFC 粉体，并研究其晶体结构、电导率、缺陷化学性质和电化学性能。制备的材料为具有 $R$-3$c$ 空间群的六方结构，在模拟工作条件下具有良好的化学稳定性。Mo 掺杂后，材料的表面氧空位浓度增加，促进了氧的传输，从而降低极化电阻($R_{pol}$)和活化能($E_a$)。其中，LSFNM$_{0.05}$ 在 700 ℃时的极化电阻最低，约为 0.26 Ω·cm$^2$。在相同温度下，LSFNM$_{0.05}$ 的最大功率密度为 484 mW/cm$^2$，优于 LSFN (353 mW/cm$^2$)和 LSFNM$_{0.1}$ (365 mW/cm$^2$)的最大功率密度。

**关键词**：质子传导型固体氧化物燃料电池；质子传输；空气电极；掺杂工程；电化学性能；氧空位

**(Edited by Wei-ping CHEN)**